Precision Spectroscopy of Molecular Hydrogen Ions: Towards Frequency Metrology of Particle Masses*

Bernhard Roth[1], Jeroen Koelemeij[1], Stephan Schiller[1], Laurent Hilico[2,3], Jean-Philippe Karr[2,3], Vladimir Korobov[4], and Dimitar Bakalov[5]

[1] Institut für Experimentalphysik, Heinrich-Heine-Universität Düsseldorf 40225 Düsseldorf, Germany
[2] Département de Physique et Modélisation, Université d'Evry Val d'Essonne Boulevard F. Mitterrand, 91025 Evry cedex
[3] Laboratoire Kastler Brossel, Université Pierre et Marie Curie T12, Case 74, 4 place Jussieu, 75252 Paris, France
[4] Joint Institute for Nuclear Research, 141980 Dubna, Russia
[5] Institute for Nuclear Research and Nuclear Energy, Sofia 1784, Bulgaria

Abstract. We describe the current status of high-precision ab initio calculations of the spectra of molecular hydrogen ions (H_2^+ and HD^+) and of two experiments for vibrational spectroscopy. The perspectives for a comparison between theory and experiment at a level of 1 ppb are considered.

1 Introduction

The molecular hydrogen ion (MHI) is the simplest stable molecule, containing just two nuclei and a single electron. Since the birth of the field of molecular physics it has played an important role: it is on one hand an important benchmark system for detailed studies of energy levels [1], for collisions and chemical reactions between charged molecules and neutral atoms/molecules, of interactions with laser radiation and energetic charged particles, and for testing the respective theoretical descriptions. On the other hand, the MHI is also an astrophysically important molecule, involved in reaction chains leading to the production of polyatomic molecules. Over 800 publications have been written on this molecule in the last 35 years [2]. The large majority are theoretical studies.

Concerning high-resolution spectroscopy of MHIs, only a limited number of investigations have been carried out, most of which a long time ago. Radiofrequency spectroscopy of the hyperfine structure in several vibrational levels has been performed on H_2^+ trapped in a Paul trap [3]; several low-lying fundamental ro-vibrational transitions of HD^+ have been measured using laser spectroscopy on an ion beam [4], while rotational and ro-vibrational transitions of H_2^+, D_2^+ and HD^+ close to the dissociation limit were investigated using microwave and laser spectroscopy, also on an ion beam [5,6]. The highest spectroscopic accuracies reported so far were achieved in the experiments of Jefferts and of Wing *et*

* This text will appear in "Precision Physics of Simple Atomic Systems", *Lecture Notes in Physics*, Springer, 2007

al. [4,7], $\simeq 1 \cdot 10^{-6}$ in relative units. Recently, also the dissociation energies have been obtained with accuracies $\simeq 1 \cdot 10^{-6}$ [8]. Thus, the experimental accuracies have been far less than those achieved in hydrogen or helium spectroscopy.

In the late 1990s, it was recognized that there are attractive reasons and many opportunities to study MHIs in novel ways and to achieve a much higher precision than previously possible [9]. Several techniques, not used before on MHIs, appeared to be applicable, including translational cooling, internal cooling, spectroscopy with reduced Doppler broadening, Doppler-free spectroscopy, high sensitivity ion detection. Novel laser systems not available at the time of the last precision spectroscopic studies can be used advantageously, among them diode lasers, quantum cascade lasers and the femtosecond frequency comb. The prospect of significantly improved experimental precision has also motivated us to develop more extended theoretical treatments of the MHI; in the course of these efforts, the accuracy of the energy levels has been increased by approximately two orders of magnitude compared to previous work.

Some of the above techniques have by now been implemented, and are reported here; the remaining appear to be feasible in the near future. These recent developments open up a number of novel applications of MHIs:

(i) test advanced *ab initio* molecular calculations (in particular, QED contributions)
(ii) measure certain fundamental constants
(iii) test concepts for the manipulation of molecules (state preparation, alignment)
(iv) sense fields (blackbody radiation [10])
(v) probe fundamental physics laws (e.g. Lorentz Invariance [11], time invariance of fundamental constants [12,13])
(vi) study electric dipole interactions between molecules [14]
(vii) explore elastic, reactive and charge exchange collisions with neutral atoms and molecules at ultralow collision energies

The successful demonstration of manipulation of MHIs at the quantum state level could also open up the possibility to study collisions with quantum-state resolution, i.e. where all parent particles are in specific quantum states.

An attractive perspective of our work pursued under (i) is to eventually determine the ratios of electron-to-proton mass (m_e/m_p), proton-to-deuteron mass (m_p/m_d) and proton-to-triton mass (m_p/m_t) from a comparison between accurate experimental and theoretical energy level data. The basis for this possibility is the dependence of the vibrational and rotational transition frequencies on the fundamental constants. For fundamental vibrational and rotational transitions, the frequencies scale approximately as

$$h\,\nu_{vib} \sim \sqrt{m_e/\mu}\,R_\infty\,, \qquad h\,\nu_{rot} \sim (m_e/\mu)R_\infty\,, \tag{1}$$

where $\mu = M_1 M_2/(M_1 + M_2)$ is the reduced mass of the two nuclei and R_∞ is the Rydberg energy. The precise dependencies have been computed in refs.

[12,15,16]. The mass ratios m_p/m_d, m_p/m_t and m_e/m_p are conventionally determined by Penning ion trap mass spectrometry on single particles or by electron spin resonance of single hydrogen-like ions in a Penning ion trap. Relative accuracies are currently $2.0 \cdot 10^{-10}$ [17], $2 \cdot 10^{-9}$, and $4.6 \cdot 10^{-10}$ [17,18], respectively. Note that in case of m_e/m_p, the determination involves the use of QED [19]. Clearly, the corresponding accuracies of ν_{vib}, ν_{rot} represent the goal levels for our ongoing experimental and theoretical efforts on H_2^+ and HD^+.

Several aspects support the expectation that such accuracies can be reached in the near future. First, the lifetimes of vibrational levels are long, the shortest ones occurring for low-lying levels in HD^+, $\simeq$ 10 ms. The relative linewidth due to spontaneous decay is thus of the order or smaller than 10^{-13}. Second, Doppler broadening can be strongly reduced or eliminated by either cooling the molecular ions or by performing two-photon Doppler-free spectroscopy. Finally, collision broadening and time-of-flight broadening can also be minimized by both cooling and providing a good ultra-high vacuum environment. Systematic shifts due to light fields, trap electric fields, and trap and environmental magnetic fields will need to be considered; hereby it will be helpful that these influences be calculated accurately, using the relative simplicity of the MHI. The theoretical determination of the energy levels at the goal accuracy level will need as input nuclear properties such as the proton and deuteron nuclear radii, which may be obtained e.g. from hydrogen spectroscopy or nuclear scattering experiments.

In this contribution we present an overview of our theoretical and experimental results achieved recently on MHIs. Chapter 2 describes the theoretical approaches for a precise computation of energy levels, including hyperfine and QED effects and the computation of one- and two-photon spectra. Chapter 3 presents the development and results from an experiment for trapping and spectroscopy of H_2^+ performed at the Université d'Evry Val d'Essonne. Chapter 4 summarizes an experiment on HD^+ at the University of Düsseldorf.

2 *Ab initio* theory of H_2^+ and HD^+

The dissociation energies of 462 states in H_2^+ and 619 in HD^+ in a wide range of v and L, vibrational and rotational quantum numbers, have been calculated some time ago by R.E. Moss [20,21] with a relative accuracy of $\sim 5 \cdot 10^{-9}$ (including the leading order relativistic and radiative corrections). Later the numerical precision of the nonrelativistic energies have been improved up to $10^{-15} - 10^{-24}$ a.u. [12,15,22–26] by using variational methods. The ultimate accuracy of $\sim 10^{-24}$ a.u. has been obtained for the H_2^+ ground state [26]. These calculations demonstrate that at least the nonrelativistic ro-vibrational transition frequencies can be determined with an uncertainty well below the 1 kHz level. In this section we describe the calculation of QED corrections as an expansion in terms of α, the fine structure constant. The numerical method exploits a variational approach based on the Slater-type exponents as basis functions. We demonstrate that the frequencies of ro-vibrational transitions can be obtained in this way with a precision better than 1 part per billion (ppb).

2.1 Variational expansion

The variational bound state wave functions are calculated by solving the three-body Schrödinger equation with Coulomb interaction using the variational approach based on the exponential expansion with randomly chosen exponents. Details and the particular strategy of choice of the variational nonlinear parameters and basis structure that have been adopted in the present work can be found in [23].

Briefly, the wave function for a state with a total orbital angular momentum L and of a total spatial parity $\pi = (-1)^L$ is expanded as follows:

$$\begin{aligned} \Psi^{\pi}_{LM}(\mathbf{R},\mathbf{r}_1) &= \sum_{l_1+l_2=L} \mathcal{Y}^{l_1 l_2}_{LM}(\hat{\mathbf{R}},\hat{\mathbf{r}}_1) G^{L\pi}_{l_1 l_2}(R,r_1,r_2), \\ G^{L\pi}_{l_1 l_2}(R,r_1,r_2) &= \sum_{n=1}^{N} \Big\{ C_n \,\mathrm{Re}\big[e^{-\alpha_n R-\beta_n r_1-\gamma_n r_2}\big] \\ &\qquad + D_n \,\mathrm{Im}\big[e^{-\alpha_n R-\beta_n r_1-\gamma_n r_2}\big] \Big\}. \end{aligned} \tag{2}$$

Here $\mathcal{Y}^{l_1 l_2}_{LM}(\hat{\mathbf{R}},\hat{\mathbf{r}}_1) = R^{l_1} r_1^{l_2} \{Y_{l_1} \otimes Y_{l_2}\}_{LM}$ are the solid bipolar harmonics, $\mathbf{R}$ is the position vector of nucleus 2 relative to nucleus 1, and $\mathbf{r}_1$, $\mathbf{r}_2$ are positions of an electron relative to nuclei 1 and 2, respectively. The complex exponents, α, β, γ, are generated in a pseudorandom way.

When the exponents α_n, β_n, and γ_n are real, the method reveals slow convergence for molecular type Coulomb systems. The use of complex exponents allows to reproduce the oscillatory behaviour of the vibrational part of the wave function and to improve convergence [27,23].

The advantage of choice (2) is the simplicity of the basis functions. It allows evaluating analytically matrix elements of the Breit-Pauli Hamiltonian and the leading-order radiative corrections and, more importantly, to treat in a systematic way the singular integrations encountered in higher-order contributions [28].

2.2 Leading-order relativistic and radiative corrections

Relativistic corrections of the leading $R_\infty \alpha^2$ order, the Breit-Pauli Hamiltonian, are well known and can be found in many textbooks [29,30]. The nuclear finite size effects are considered as contributions to this order. Details, relevant particularly to the case of the MHIs, can be found in [31].

In what follows we assume that the nuclear charges are $Z_1 = Z_2 = Z = 1$ and nuclear masses are denoted by capital M. The units adopted are ($\hbar = e = m_e = 1$).

The radiative corrections of an order $R_\infty \alpha^3$ for a one electron molecular system can be expressed by the following set of equations (see Refs. [32–34]).

The one-loop self-energy correction (orders $R_\infty\alpha^3$ and $R_\infty\alpha^3(m/M)$) is:

$$\begin{aligned} E^{(3)}_{se} = {} & \frac{4\alpha^3 Z}{3}\left(\ln\frac{1}{\alpha^2} - \beta(L,v) + \frac{5}{6} - \frac{3}{8}\right)\langle\delta(\mathbf{r}_1)+\delta(\mathbf{r}_2)\rangle\,, \\ & +\alpha^3 Z^2 \sum_{i=1,2}\left[\frac{2}{3M_i}\left(-\ln\alpha - 4\,\beta(L,v) + \frac{31}{3}\right)\langle\delta(\mathbf{r}_i)\rangle - \frac{14}{3M_i}Q(r_i)\right], \end{aligned} \tag{3}$$

where

$$\beta(L,v) = \frac{\langle \mathbf{J}(H_0 - E_0)\ln\left((H_0-E_0)/R_\infty\right)\mathbf{J}\rangle}{\langle[\mathbf{J},[H_0,\,\mathbf{J}]]/2\rangle} \tag{4}$$

is the Bethe logarithm. The latter quantity presents the most difficult numerical problem in computation of QED corrections for the three-body bound states. In [34,35] the calculations for a wide range of ro-vibrational states in H_2^+ and HD^+ have been performed to an accuracy of about 7 significant digits. The operator $\mathbf{J}$ in (4) is the electric current density operator of the system[1]. The last term, $Q(r)$, in Eq. (3) is the mean value of a regularized operator introduced by Araki and Sucher [36] for the $1/(4\pi r^3)$ potential:

$$Q(r) = \lim_{\rho\to 0}\left\langle \frac{\Theta(r-\rho)}{4\pi r^3} + (\ln\rho + \gamma_E)\delta(\mathbf{r})\right\rangle. \tag{5}$$

The values of this matrix element for ro-vibrational states are calculated in [31].

The remaining contributions in this order can be obtained from the Pauli form factor of an electron (anomalous magnetic moment):

$$E^{(3)}_{anom} = \pi\alpha^2 Z\left[\frac{1}{2}\left(\frac{\alpha}{\pi}\right)\right]\langle\delta(\mathbf{r}_1)+\delta(\mathbf{r}_2)\rangle\,. \tag{6}$$

and from the one-loop vacuum polarization:

$$E^{(3)}_{vp} = \frac{4\alpha^3 Z}{3}\left[-\frac{1}{5}\right]\langle\delta(\mathbf{r}_1)+\delta(\mathbf{r}_2)\rangle\,. \tag{7}$$

2.3 $R_\infty\alpha^4$ order corrections in the nonrecoil limit

The contribution of recoil corrections, proportional to (m/M), in the $R_\infty\alpha^4$ order are too small for our present consideration and may be neglected. Radiative corrections for a bound electron in an external field are known analytically

[1] $\mathbf{J} = \sum_a z_a\mathbf{p}_a/m_a$, where z_a, $\mathbf{p}_a$, m_a are the charge, impulse, and mass of a particle a. The sum is performed over all particles of the system.

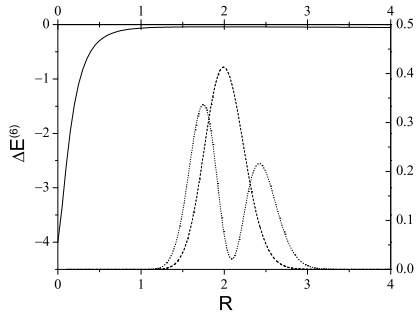

Fig. 1. Adiabatic potential of the $m\alpha^6$ order contribution to the Dirac energy of the two-center problem ($Z_1 = Z_2 = 1$). Dashed curves are the squared densities of the ground and first vibrational state wave functions of H_2^+ ion.

[38,39]:

$$
\begin{aligned}
E^{(4)}_{se} &= \alpha^4 Z^2 \left[4\pi \left(\frac{139}{128} - \frac{1}{2}\ln 2\right)\right] \langle \delta(\mathbf{r}_1) + \delta(\mathbf{r}_2)\rangle \,, \\
E^{(4)}_{vp} &= \alpha^4 Z^2 \left[\frac{5\pi}{48}\right] \langle \delta(\mathbf{r}_1) + \delta(\mathbf{r}_2)\rangle \,, \\
E^{(4)}_{anom} &= \alpha^2 Z\pi \left[\left(\frac{\alpha}{\pi}\right)^2 \left(\frac{197}{144} + \frac{\pi^2}{12} - \frac{\pi^2}{2}\ln 2 + \frac{3}{4}\zeta(3)\right)\right] \langle \delta(\mathbf{r}_1) + \delta(\mathbf{r}_2)\rangle \,, \\
E^{(4)}_{2loop} &= \alpha^2 Z\pi \left[\left(\frac{\alpha}{\pi}\right)^2 \left(-\frac{6131}{1296} - \frac{49\pi^2}{108} + 2\pi^2 \ln 2 - 3\zeta(3)\right)\right] \langle \delta(\mathbf{r}_1) + \delta(\mathbf{r}_2)\rangle \,.
\end{aligned}
\tag{8}
$$

The last equation includes both the Dirac form factor and polarization operator contributions.

The $R_\infty \alpha^4$ relativistic correction is obtained using the adiabatic "effective" potential for an $m\alpha^6$ term in the α expansion of the two-center Dirac energy (see Fig. 1). Averaging over the squared wave function density of a state one gets $E^{(4)}_{rc}$. The adiabatic potentials have been obtained recently with about 5 significant digits [37], and the Born-Oppenheimer solution yields approximate wave functions at the $(m/M) \approx 10^{-4}$ level, which allows to claim that $E^{(4)}_{rc}$ is now known to 4 digits.

Some higher order radiative corrections for a bound electron in an external field are also known in an analytic form [38,39] and can be included into consideration:

$$
E^{(5)}_{se} = \alpha^5 Z^3 \, \ln^2 (Z\alpha)^{-2} \big[-1\big] \, \langle \delta(\mathbf{r}_1) + \delta(\mathbf{r}_2)\rangle \,. \tag{9}
$$

The electron ground state wave function may be approximated by $\psi_e(\mathbf{r}_e) = C[\psi_{1s}(\mathbf{r}_1) + \psi_{1s}(\mathbf{r}_2)]$, where ψ_{1s} is the hydrogen ground state wave function and C is a normalization coefficient. Thus, one may use this approximation to

evaluate other contributions in the $R_\infty\alpha^5$ order:

$$
\begin{aligned}
E^{(5')}_{se} &= \alpha^5 Z^3 \Big[A_{61}\ln(Z\alpha)^{-2} + A_{60}\Big]\,\langle\delta(\mathbf{r}_1)+\delta(\mathbf{r}_2)\rangle\,,\\
E^{(5)}_{2loop} &= \frac{\alpha^5}{\pi} Z^2 \big[B_{50}\big]\,\langle\delta(\mathbf{r}_1)+\delta(\mathbf{r}_2)\rangle\,,
\end{aligned}
\tag{10}
$$

where the constants A_{61}, A_{60}, and B_{50} are taken equal to the constants of the $1s$ state of the hydrogen atom $A_{61} = 5.419\ldots$ [40], $A_{60} = -30.924\ldots$ [41], and $B_{50} = -21.556\ldots$ [42] (see also Ref. [39] and references therein). The final theoretical uncertainty in the transition frequency (see Table 1) is determined by the total contribution of the last two equations.

2.4 Hyperfine structure of states

The leading order contribution to the hyperfine splitting of the ro-vibrational states is calculated using the spin-dependent part of the Breit-Pauli interaction Hamiltonian, with phenomenological values for the nuclear magnetic moments and the electron anomalous magnetic moment. The hyperfine levels of HD^+, E_{vLFSJ}, are labelled with the quantum numbers F, S and J of the intermediate angular momenta $\mathbf{F} = \mathbf{I}_p + \mathbf{s}_e$, $\mathbf{S} = \mathbf{F} + \mathbf{I}_d$ and of the total angular momentum $\mathbf{J} = \mathbf{L} + \mathbf{S}$ [43]. In case of H_2^+ due to Pauli exclusion principle the total nuclear spin I is uniquely defined by L and parity of the electronic state. The following coupling scheme is adopted: $\mathbf{F} = \mathbf{I} + \mathbf{s}_e$ and $\mathbf{J} = \mathbf{L} + \mathbf{F}$ [44]. The hyperfine structure (HFS) of the ro-vibrational states of HD^+ consists of 4, 10 or 12 hyperfine sub-levels for $L=0$, $L=1$ and $L\geq 2$, respectively (see Fig. 2). The multiplicity of the HFS of H_2^+ is reduced to 1 for $L=0$, 5 for $L=1$, 2 for even, and 6 for odd L states. Typically, the hyperfine splitting of the lower ro-vibrational states of HD^+ and H_2^+ is about 1 GHz. The uncertainty in the hyperfine spectrum is related to the unknown contribution of the spin interaction terms of orders $O(R_\infty\alpha^4(m/M))$ and higher, which have not yet been taken into consideration, and is estimated not to exceed 100 kHz.

Each transition line between ro-vibrational states is split into a multiplet of hyperfine components, corresponding to the allowed transitions $i \to f$ between

Table 1. Summary of contributions to the $(v=0, L=0) \to (v'=1, L'=0)$ transition frequency (in MHz).

	H_2^+	HD^+
ΔE_{nr}	65 687 511.0686	57 349 439.9717
ΔE_{α^2}	1091.041(03)	958.152(03)
ΔE_{α^3}	−276.544(02)	−242.118(02)
ΔE_{α^4}	−1.997	−1.748
ΔE_{α^5}	0.120(23)	0.106(19)
ΔE_{tot}	65 688 323.688(25)	57 350 154.368(21)

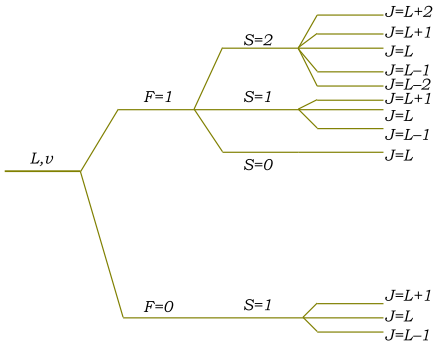

Fig. 2. Hyperfine structure of a ro-vibrational state of HD^+ with $L \geq 2$.

the states of the hyperfine structure of the initial and final states. Whether these hyperfine components will be resolved or the spectrum profile depends on the initial and final state lifetime and on the experimental conditions (transition linewidth Γ_f, laser intensity I, temperature, interaction time etc.) Examples of spectral data are presented in experimental sections of our review (see Fig. 13). The shape of the profile also depends on the population of the initial hyperfine states. The general expressions for the probability per unit time for one- and two-photon transitions between ro-vibrational states of the MHIs with account of the hyperfine structure are given in Ref. [45].

The probability per unit time for the hyperfine transition $i \to f$ at resonance (averaged over the magnetic numbers of initial and final states), $\Gamma_{f,i}$, may be represented in the form:

$$\Gamma_{f,i} = T_{f,i}^2 \, \Gamma_{v'L',vL}, \qquad \Gamma_{v'L',vL} = \frac{2\pi\alpha}{3\hbar} \, \frac{I}{\Gamma_f} \, \frac{\langle v'L' || \, \mathbf{d} \, || vL \rangle^2}{2L+1}. \tag{11}$$

Here $\Gamma_{v'L',vL}$ is the probability per unit time of laser-stimulated dipole transitions between ro-vibrational states, $\langle v'L' || \, \mathbf{d} \, || vL \rangle$ is the reduced matrix element of the electric dipole moment of the HD^+ ion $\mathbf{d} = \sum_a z_a \mathbf{r}_a$, and

$$T_{f,i} = \sqrt{(2J'+1)(2L+1)} \sum_{F''S''} (-1)^{S''+J+L'} \left\{ \begin{array}{ccc} L & 1 & L' \\ J' & S'' & J \end{array} \right\} \beta^f_{F''S''} \beta^i_{F''S''}, \tag{12}$$

where $\beta^{vLFSJ}_{F''S''}$ are constant amplitudes of the state vectors of the hyperfine states:

$$|vLFSJ, J_z\rangle = \sum_{F''S''} \beta^{vLFSJ}_{F''S''} \sum_{M\zeta} C^{JJ_z}_{LM,S''\zeta} \Psi_{vLM}(\mathbf{R}, \mathbf{r}_1) \chi(F''S'', \zeta), \tag{13}$$

determined from the effective Hamiltonian of spin interaction. Here $\chi(FS, \zeta)$ are basis spinors of definite values of F, S and S_z in the space of the spin variables. The relative intensity of the hyperfine components of a transition line

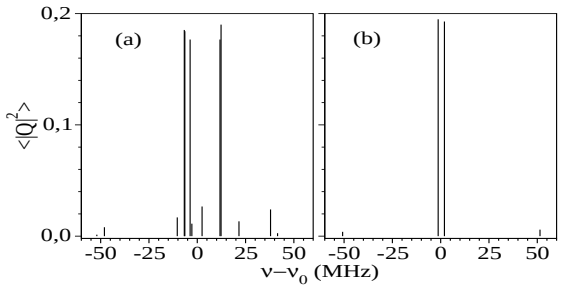

Fig. 3. Hyperfine splitting and intensities of the two-photon ro-vibrational transition line for the H_2^+ ion: (a) $(v=0, L=1) \to (v'=1, L'=1)$, (b) $(v=0, L=2) \to (v'=1, L'=2)$.

between ro-vibrational states is thus determined by the amplitudes $T_{f,i}$. In case the individual hyperfine components cannot be resolved, the observable intensity is reduced to the intensity of the dipole ro-vibrational transition $\Gamma_{v'L',vL}$, in agreement with the identity $\sum_f T_{f,i}^2 = 1$.

The hyperfine structure of the one- and two-photon transition lines includes a large number of components, most of which, however, are suppressed. There are as well dominant (or "*favoured*") transitions between states with similar spin structure, such as $(vLFJ) \to (v'L'FJ')$ with $\Delta J = \Delta L$ (for H_2^+). In such pairs of homologous hyperfine states the spin-dependent corrections to the ro-vibrational energies $E_{v'L'FJ'}$ and E_{vLFJ} have close values, which partially cancel each other when evaluating the spin correction to the resonance transition frequency $(E_{v'L'FJ'} - E_{vLFJ})/h$. Indeed, the *favoured* hyperfine transitions span over a frequency interval less than 25 MHz (see Fig 3). It is natural to expect that the unknown contributions to the frequency of the favoured transitions from the spin interactions of order $R_\infty \alpha^4 (m/M)$ and higher also tend to cancel each other; therefore, the theoretical uncertainty of the resonance frequency of the *favoured* hyperfine sublines will be less than ~ 5 kHz.

2.5 Two-photon transition probabilities

In order to assess the feasibility of Doppler-free two-photon spectroscopy in H_2^+ or HD^+, it is essential to evaluate transition probabilities between ro-vibrational states. This can be done using the formula from second-order perturbation theory [46], and the accurate wavefunctions provided by variational calculations. Assuming that magnetic sublevels are equally populated, the two-photon transition probability at resonance between states v, L and v', L' is

$$\Gamma_{v,L,v',L'} = \left(\frac{4\pi a_0^3}{\hbar c}\right)^2 \frac{4I^2}{\Gamma_f} \overline{Q}_{v,L,v',L'} \tag{14}$$

where I is the excitation intensity, Γ_f the transition linewidth, and

$$\overline{Q}_{v,L,v',L'} = \frac{1}{2L+1} \sum_{k=0,2} \frac{\left|\langle vL \| Q^{(k)} \| v'L' \rangle\right|^2}{2k+1}. \tag{15}$$

$Q^{(0)}$, $Q^{(2)}$ are respectively the scalar and tensor parts of the two-photon transition operator

$$Q = \frac{1}{4\pi\epsilon_0 a_0^3}\,\mathbf{d}\cdot\boldsymbol{\epsilon}\,\frac{1}{E-H}\,\mathbf{d}\cdot\boldsymbol{\epsilon} \tag{16}$$

Here, $E = [E(v,L) + E(v',L')]/2$ is the one-photon resonance energy and $\boldsymbol{\epsilon}$ the exciting field polarization. The two-photon transition probabilities were calculated in [22,47].

For the H_2^+ case [47] there exists a quasi-selection rule $\Delta v = \pm 1$, and the dimensionless transition probabilities $\overline{Q}_{v,L,v',L'}$ are rather small, of the order of 1, which is due to the level structure of H_2^+. If we consider the example of transitions between $L = 0$ states, these states are of ${}^1S^e$ symmetry, and there is no resonant intermediate level of ${}^1P^o$ symmetry that could enhance the transition probability.

The situation is different in the HD^+ case [22], since there is no splitting between singlet and triplet state due to the loss of exchange symmetry between the nuclei. As a result, for a transition between $L = 0$ (S^e) states, there exist intermediate bound P^o levels which can be very close in energy and efficiently enhance the transition probability. This is most likely to happen if the difference between v and v' (the initial and final vibrational quantum numbers) is an even number. In this case, the state $(v'' = (v+v')/2, L'' = L \pm 1)$ is often close to the middle energy $E = [E(v,L) + E(v',L')]/2$, because of the quasi-harmonic structure of vibrational levels. As a result, some of the most intense two-photon lines are $\Delta v = 2$ transitions in the 5-6 μm range or $\Delta v = 4$ transitions in the 2.5-3 μm range, accessible e.g. with continuous-wave optical parametric oscillator or quantum cascade lasers. The dimensionless transition probabilities $\overline{Q}_{v,L,v',L'}$ can reach values as high as 300 for the $(v=0, L=1) \to (v=2, L=1)$ transition at 5.366 μm. Thus, the HD^+ molecular ion is a promising candidate for precise two-photon spectroscopy.

The next step is to consider the hyperfine structure of two-photon transition lines. The representation of the hyperfine state vectors in the H_2^+ case is

$$|vLFJJ_z\rangle = \sum_{F'} \beta_{F'}^{vLFJ} \sum_{M\zeta} C_{LM,F'\zeta}^{JJ_z}\,\psi_{vLM}(\mathbf{R},\mathbf{r_1})\,\chi(F',\zeta). \tag{17}$$

The definitions for $\chi(F',\zeta)$ and $\beta_{F'}^{vLFJ}$ are similar to those in (13). Assuming equal populations for hyperfine magnetic sublevels, the dimensionless transition probability between levels $|i\rangle = |vLFJ\rangle$ and $|f\rangle = |v'L'F'J'\rangle$ is:

$$\overline{Q}_{i,f} = (2J'+1) \sum_{k=0,2} \frac{\left| \langle vL\|Q^{(k)}\|v'L'\rangle \sum_{F''} (-1)^{J'+L+F''} \begin{Bmatrix} L & k & L' \\ J' & F'' & J \end{Bmatrix} \beta_{F''}^{f} \beta_{F''}^{i} \right|^2}{2k+1} \tag{18}$$

The hyperfine structure of two different transitions for linear polarization is shown in Fig. 3. Transitions between odd L states (Fig. 3(a)) comprise between 25 to 34 components, 5 or 6 of which are favoured. Transitions between even

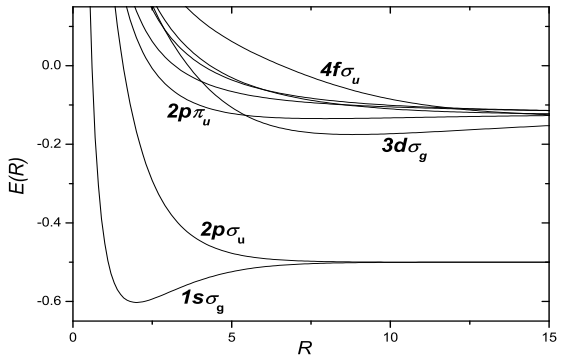

Fig. 4. Born-Oppenheimer electronic energies (in a.u.) of the adiabatic potential terms.

L states (Fig. 3(b)) have a much simpler structure, the total nuclear spin being zero. The non zero even L spectrum comprises only two main components (verifying $\Delta J = 0$) together with two weak satellites. Transitions between $L = 0$ states are structureless, which makes them especially attractive from a metrological point of view.

3 Two-photon spectroscopy of H_2^+

A two-photon vibrational spectroscopy experiment aimed at the determination of the electron to proton mass ratio is being setup at the Kastler Brossel Laboratory. We begin by recalling the basic spectral features of the MHI, and discuss the planned experimental sequence. In the second part, we report on the present status of the experimental setup. It is composed of a hyperbolic Paul trap in which a few thousand H_2^+ ions can be confined, a UV laser for ion preparation and detection by state-selective photodissociation, and a narrow-line, tunable laser system that will excite the two-photon transition.

3.1 H_2^+ level structure

Although the Born Oppenheimer (BO) approximation is not relevant for highly accurate calculations, it remains a very convenient tool to get a useful insight into the H_2^+ level structure. In order to understand the processes discussed here, it is enough to consider the first two BO electronic curves: the ground state $1s\sigma_g$ and first excited state $2p\sigma_u$, which are depicted in Fig. 4.

The exact symmetries of the system are the total spatial parity π and the exchange of nuclei P_{12}; the g/u electronic parity π_e used in the BO approach is related to them by $\pi_e = \pi P_{12}$. The bound levels of H_2^+ can be labelled $v, (^{2I+1}L^{e,o})$ where v and L are the vibrational and orbital quantum numbers, I is the total nuclear spin quantum number and (e, o) stands for the total parity. Since the total spatial parity is $\pi = (-1)^L$, the $1s\sigma_g$ curve only supports $^1S^e$, $^3P^o$, $^1D^e \ldots$ levels.

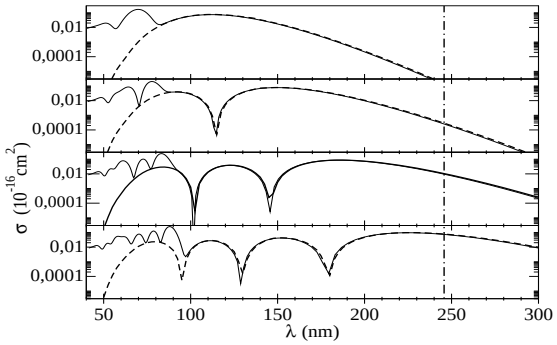

Fig. 5. Photodissociation cross sections of the $L=0$, v levels of H_2^+. The dashed lines are the result of a Born Oppenheimer calculation [50], which takes the $1s\sigma_g$ and $2p\sigma_u$ electronic curves into account. The nodal structure of the cross section reflects that of the vibrational wavefunction. The solid lines are obtained from an exact variational method which fully takes into account the three body dynamics [51]. The additional nodal structure appearing in the short wavelength domain can be interpreted as the photodissociation to higher excited electronic states ($3d\sigma_g$, $2p\pi_u$, $4f\sigma_u$, ...). The dot-dashed vertical line corresponds to the KrF laser wavelength of 248 nm.

The $2p\sigma_u$ electronic curve presents at large internuclear distances a weak attractive potential that supports two bound $L = 0$ energy levels [20,48]. Some of those states have been observed by microwave or laser spectroscopy experiments [49]. At higher L the $2p\sigma_u$ potential supports bound or dissociative $^1P^o$, $^3D^e$ $^1F^o$ ... states that can be calculated numerically using either the variational, or the complex coordinate rotation method.

3.2 One-photon transitions: photodissociation

The selection rules for one-photon dipole transitions are $\Delta L = \pm 1$ and $\Delta I = 0$. As a consequence, transitions between bound ro-vibrational states of H_2^+ are forbidden (in contrast with the HD^+ case), resulting in very long-lived states. On the other hand, one-photon photodissociation transitions from $1s\sigma_g$ to $2p\sigma_u$ electronic states are allowed. The photodissociation cross sections σ_v of the $(^1S^e, v)$ states have been first computed by Dunn [50] in the Born-Oppenheimer approximation, and then using the perimetric coordinate variational method in [51]. The results are given in Fig. 5. They show that a laser source in the 250 nm range can be used to selectively photodissociate the $v = 1, 2, 3, \ldots$ vibrational states while keeping the ions in the $v = 0$ level since the successive cross section ratios σ_{v+1}/σ_v are 214, 40, 10, for $v = 0, 1, 2$, respectively.

3.3 Two-photon transitions: choice of the transition

One-photon transitions between bound states being forbidden, a high resolution study of the vibrational structure of H_2^+ is only possible using Doppler-free two-photon spectroscopy. Two-photon transitions obey the selection rule $\Delta L = 0, \pm 2$

as well as the quasi selection rule $\Delta v = \pm 1$, as discussed in section 2.5. The corresponding $(v, L) \rightarrow (v' = v+1, L')$ transition frequencies lie in the 8-12 μm range. Among them, we have chosen to probe the $v=0 \rightarrow v=1$ transitions, for L and L' equal to 0 or 2 and eventually 1 or 3. We now give the arguments that explain this choice.

The first condition to fulfill is that it should be possible to prepare a large enough number of H_2^+ in the initial state of the transition. The ro-vibrational populations of H_2^+ ions, after creation by electron impact ionization of a low pressure H_2 gas, have been studied both theoretically and experimentally [52]. The vibrational populations are linked to the overlap of the H_2 and H_2^+ vibrational wave functions (Franck-Condon principle); they are found to be of the order of 12, 18, 18, 15, 11, 8, 5, 4% for the first few levels. The rotational populations of the H_2^+ ions are those of the H_2 mother molecules, i.e. 12, 28, 28, 18, 8% at 300 K. Moreover, we have shown in the previous paragraph that UV photodissociation provides a convenient way to prepare ions in the ground vibrational state; it is then desirable to choose a $v=0$ state as initial state of the transition, with L between 0 and 3, $L=1$ or 2 being the best choices with respect to the number of ions. The same photodissociation process can be used to detect the ions in the excited $v=1$ state.

The hyperfine structure of two-photon lines should also be considered; it is apparent from Fig. 3 that it is simpler for transitions between even L states. Interpretation of experimental data is likely to be easier in this case.

The intensities of the various $(v = 0, L) \rightarrow (v' = 1, L')$ (with low L) two-photon lines are of the same magnitude; the choice of a particular transition depends mostly on the availability and characteristics of laser sources at the required wavelength. The whole mid-infrared range is accessible by the recently developed quantum cascade lasers (QCL); $L' = L$ transitions are especially attractive, because they lie within the spectrum of CO_2 lasers ($\lambda \simeq$ 9-10 μm). Also, a number of frequency reference molecular absorption lines are known in this range [53]. The first transition that is going to be probed in our experiment is the $(v = 0, L = 2) \rightarrow (v' = 1, L' = 2)$ line at 9.166 nm. The details of coincidences with CO_2 lines and molecular reference lines, which make this transition favorable, are explained below.

3.4 Experimental sequence

The two-photon transition matrix elements $|Q_{v,L,v',L'}|^2$ of the "favoured" hyperfine components of two-photon transitions are of the order of 0.2 (see Fig. 3). A typical QCL can deliver about 50 mW of single-mode optical power. Assuming a perfect coupling to a build-up cavity of finesse 1000 with a waist of 1 mm, one obtains a laser flux of 15 W/mm^2. Assuming an instrumental width $\Gamma_f \approx$10 kHz, equation (14) yields transition rates of about 70/s. This order of magnitude shows that long interaction times are needed and that one has to work with a cloud of trapped ions, having a radius of the order of the beam waist.

The considerations of the previous paragraph show that vibrational two-photon spectroscopy of H_2^+ can be performed by $(2+1')$ resonance enhanced

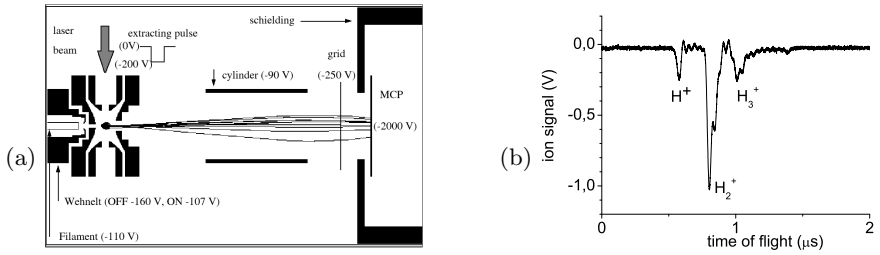

Fig. 6. (a) Simulation of the experimental setup for ion creation, trapping and detection using the SIMION7 software. MCP is a multichannel plate detector. (b) Time of flight spectrum showing the H^+, H_2^+ and H_3^+ species confined in the Paul trap.

multiphoton dissociation (REMPD). This process is very similar to that implemented for HD^+ vibrational spectroscopy and described in more detail in Section 4.

The experiment will be conducted in the following stages:

- simultaneous creation, trapping and selection of $(L, v = 0)$ H_2^+ ions.
- excitation of the $(L, v=0) \rightarrow (L', v'=1)$ two-photon transition.
- photodissociation of the $(L, v=1)$ H_2^+ ions.
- time of flight detection of H^+ and H_2^+ ions.

3.5 Experimental setup

The ion trap is depicted in Fig. 6(a). It is a hyperbolic Paul trap with a ring of inner radius $r_0 = 8.2$ mm and two end caps separated by $2z_0 = 6$ mm. Two pairs of holes (2 mm in diameter) are drilled in the ring along two orthogonal axes to shine the ion cloud with the UV and IR light. Both end cap electrodes are AC grounded. A RF voltage (about 200 V peak to peak amplitude at 10.3 MHz) and a continuous voltage of a few Volts are applied to the ring electrode, resulting in trapping well depths of a few eV.

The H_2^+ ions are produced by electron impact ionisation from the residual H_2 gas. The electron gun is made of a tungsten wire and a Wehnelt cylinder; it is typically turned on for 100-200 ms. A 1 mm hole in one of the end cap electrodes allows access to the trap.

The contents of the trap are analyzed by applying a short negative high voltage pulse to the second end cap, thus extracting the ions from the trap through a 2 mm hole. The extracted ions are accelerated and focused onto a multi-channel plate (MCP) detector located 7 cm away, a long enough distance to separate by time of flight the H^+, H_2^+ and H_3^+ ions that are simultaneously produced and trapped. A typical time of flight spectrum is shown in Fig. 6(b). Up to a few thousand H_2^+ ions can be stored in the trap. The ion lifetime is of a few seconds and is limited by the residual pressure in the vacuum chamber.

The undesirable H^+ and H_3^+ ions are eliminated using the parametric excitation of their secular motion, by applying RF voltage in the MHz range on one

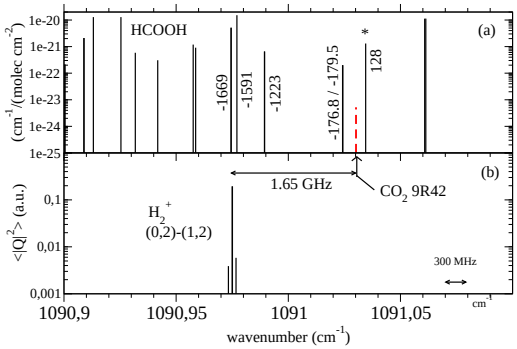

Fig. 7. (a) Absorption spectrum of formic acid (HCOOH) [53]. The line intensities are given in $\mathrm{cm}^{-1}/(\mathrm{molecule\ cm}^{-2})$. (b) Two-photon transition probabilities in atomic units. The central peak is made of two close components (see Fig. 3). The dashed line is the 9R(42) CO_2 emission line. The detunings between the 9R(42) CO_2 line and the HCOOH lines are indicated in MHz. The CO_2 laser is locked to the HCOOH line indicated by the star.

of the end cap electrodes during the ionisation process. A KrF excimer laser at 248 nm is used to photodissociate the $v \geq 1$ states in order to produce a $(L, v=0)$ ions cloud. The ions are shined by 20 mJ pulses during the filling of the trap. The characterization of ro-vibrational populations of the resulting ion cloud is now in progress.

Since all the bound states of H_2^+ are metastable, the natural widths of the two-photon transitions are extremely small. In Paul traps, the ion cloud temperature is of the order of magnitude of the potential depth expressed in K, i.e. $\approx 10^4$ K in our trap. Under those conditions, the two-photon linewidth Γ_f (appearing in Eq. (14)) is expected to be limited by the second-order Doppler effect, i.e. of the order 10 kHz. It will limit the ultimate frequency resolution of the experiment at the $3 \cdot 10^{-10}$ level, and the mass ratio resolution at the $6 \cdot 10^{-10}$ level.

Ion cooling will thus be necessary in order to reach the metrological objective of the experiment at the 10^{-10} level. Nevertheless, the first step of the experiment is the observation of a two-photon transition, which is feasible with hot ions using a kHz linewidth laser source.

3.6 Two-photon excitation laser source

The laser system we have built is aimed at exciting the $(L = 2, v = 0) \rightarrow (L' = 2, v' = 1)$ two-photon transition at 9.166 μm. In this range, two kinds of laser sources are available. Single-mode CO_2 lasers have high output power and sub-kHz linewidths, but are hardly tunable on ranges exceeding 100 MHz, i.e. much smaller than the 1.65 GHz gap between the closest CO_2 emission line (9R(42)) and the H_2^+ line (see Fig. 7(b)). Recently, single mode quantum cascade laser (QCL) became commercially available. They can be tuned over about 10 cm^{-1} (300 GHz) through their temperature and injection current, but have

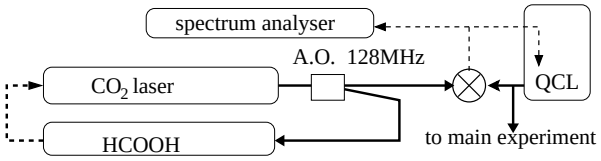

Fig. 8. Simplified setup of the CO_2/HCOOH phase-locked quantum cascade laser source. The QCL is mounted in a liquid nitrogen optical cryostat. The mixer is a room temperature HgCdZnTe detector. Solid lines are optical paths. Dashed lines are electrical paths and servo loops. A.O. is an acousto-optic modulator.

large linewidths of the order of a few MHz. Several experiments have shown that the linewidth can be reduced well below the kHz level by injection-current locking the QCL to a molecular line [54] or to a high finesse Fabry-Perot cavity resonance [55]. We have developed a laser source that takes advantage of both the narrow linewidth of the CO_2 laser and the tunability of the QCL [56].

The setup is shown in Fig. 8. A CO_2 laser oscillating on the 9R(42) line is frequency shifted by 128 MHz and stabilized on the intracavity saturated absorption signal of the $(21, 3, 19) \rightarrow (21, 2, 20)$ line of the ν_6 band of formic acid (HCOOH) (see Fig. 7(a)). The absolute frequency of that transition (32 708 263 980.5 kHz) has recently be determined with an uncertainty of 1 kHz [57] by sum frequency mixing with a 30 THz wide visible femtosecond frequency comb [58]. The QCL is operated in a liquid nitrogen optical cryostat. The output power is 50 mW with a 700 mA injection current and a temperature of 80K. The QCL is phase-locked to the CO_2 laser with a tunable frequency offset in the 500-2000 MHz range [56]. The analysis of the beat note spectrum under locked conditions (see Fig. 9) shows that we have realized a narrow-line tunable laser source well suited to probe the H_2^+ two-photon lines, and also the ro-vibrationnal

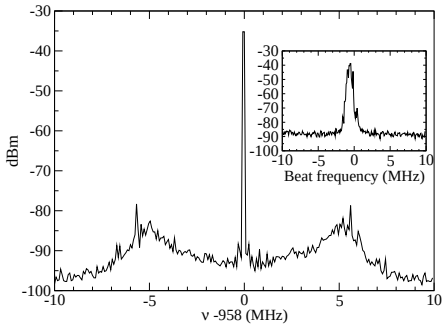

Fig. 9. Phase-locked beat note between the QCL and the CO_2/HCOOH frequency reference. RBW 10 kHz, VBW 1 kHz. The spectrum shows a loop bandwidth of the order of 6 MHz. The central peak is extremely narrow, with a -3dB width smaller than the 200 Hz resolution of the spectrum analyser. The inset shows the free running beat note with the same scale and a 500 kHz RBW.

spectrum of HCOOH [58] or other molecules (NH_3, ...) of atmospheric or astrophysical interest.

4 Cooling and Spectroscopy of HD^+

In experiments performed at the University of Düsseldorf, the MHIs H_2^+, D_2^+, and HD^+ were cooled to temperatures of $\simeq 10$ mK in a radiofrequency trap, by sympathetic cooling with laser-cooled beryllium ions. High-resolution spectroscopic studies of several rovibrational infrared transitions in HD^+ were performed. Hyperfine splitting of the lines was observed, and is in good agreement with theoretical predictions. The transitions were detected by monitoring the decrease in ion number after selective photodissociation of HD^+ ions in the upper vibrational state.

4.1 Preparation and characterization of cold MHI ensembles

MHIs are just a few of a multitude of species that can be cooled to mK temperatures, by sympathetic cooling [59,60] - the molecular species and a laser-coolable atomic species, with the same sign of charge, are simultaneously stored in a radiofrequency trap. Laser cooling the atoms then also efficiently cools the molecular ions via the long-range Coulomb interaction. Temperatures below 20 mK can be reliably reached. We have shown that using Be^+ ions as coolant permits to cool sympathetically ions from mass 1 to mass 200 amu [61–63]. A heavier atomic coolant species can be used to extend the mass range. For example, using $^{138}Ba^+$ as coolant molecular ions up to mass 410 amu have recently been cooled [64].

We use a linear quadrupole trap to simultaneously store both Be^+ and MHIs. The radiofrequency trap is driven at 14 MHz, with a peak-to-peak amplitude of 380 V. This results in a radial Mathieu stability parameter $q_r \simeq 0.13$ for HD^+. The trap is enclosed in a UHV chamber kept below 10^{-10} mbar. The chamber is equipped with a leak valve for the controlled introduction of gases. An all-solid-state 313 nm laser system is used for cooling Be^+ [65].

To load Be^+ ions into the trap, atoms are thermally evaporated from a beryllium wire, and ionised by an electron beam. The molecular loading is achieved by leaking in neutral gas at a pressure of $\sim(1\text{–}3)\cdot10^{-10}$ mbar, ionised by an electron beam with an energy of 200 eV, and a current of ~ 30 μA, for a loading time of 2 s. This produces mixed-species crystals like those shown in Figs. 10(a,b). The ions with a higher charge-to-mass ratio (in this case the molecular ions) experience a stronger trap pseudopotential, and thus form a dark (non-fluorescing) core to the crystal. The asymmetric distribution of species along the z-axis observed in Fig. 10(b) is caused by the light pressure of the cooling laser on the beryllium ions.

The observed crystals are reproduced by molecular dynamics (MD) simulations [61,66]. Visual matching of overall structure, structural details and blurrings of CCD and simulated images allows fitting the ion numbers and temperatures of the different species. The number of ions of different species given

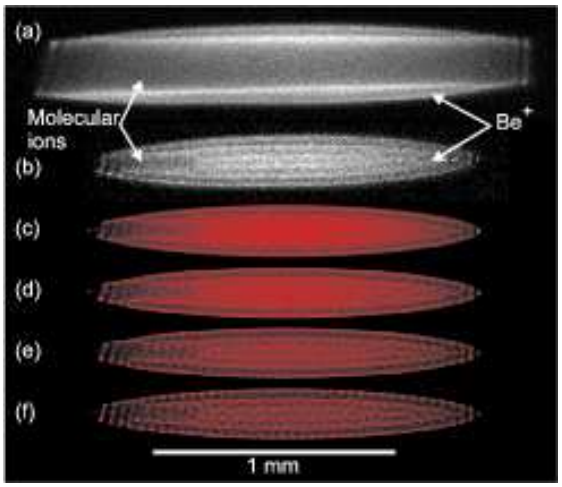

Fig. 10. Fluorescence images of (a) a large ion crystal with a high fraction of sympathetically cooled ions (approximately 1200 light ions and 800 Be^+ ions) (b) a smaller crystal containing approx. 690 Be^+ ions, and 12 (exactly) HD^+ ions, and simulated images of this crystal at (c) 20 mK, (d) 12 mK, (e) 8 mK and (f) 6 mK. In the simulations, the beryllium ions are shown in red and the HD^+ ions in blue. Laser cooling beam propagation is to the right, along the z-axis [61].

in Fig. 10(b) were found in this way. In the simulations we assume an ideal linear trap, use the quasipotential approximation and model heating effects by stochastic forces on the ions. The obtained temperatures are thus effective secular temperatures. Fig. 10 shows a determination of the temperature; agreement is found for a Be^+ temperature of appox. 10 mK. This sets an upper limit, as our experimental images are also limited in sharpness by our detection optics, CCD resolution, and sensor noise, which are not considered. The temperature varies depending on crystal size and cooling parameters, and is typically in the range 5 mK to 15 mK, with smaller crystals generally colder. These temperatures are consistent with measurements of the fluorescence lineshape of the Be^+ ions.

For all species of molecular ions studied here, our MD simulations show that the sympathetically cooled molecular ion ensemble is also crystalline, i.e. its time-averaged ion distribution is strongly inhomogeneous, and that it is strongly thermally coupled to the Be^+ ions. Assuming similar heating effects for the molecular ions and the Be^+ ions, the simulations show that the moleculars ions have a temperature similar to that of Be^+, due to the strong Coulomb coupling.

The trapped species are identified and the time evolution of their numbers is monitored by excitation of their mass-dependent radial (secular) modes, using a spatially homogenous and temporally oscillating electric field. For HD^+ ions the measured secular frequency was $\approx$770 kHz, significantly shifted from the calculated single-particle frequency, due to Coulomb coupling between different species in the trap [67]. Excitation amplitude, sweep rate, and covered frequency

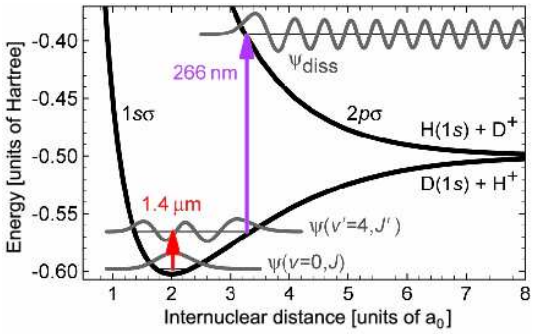

Fig. 11. Principle of $(1+1')$ REMPD spectroscopy of HD^+ ions. A tunable IR diode laser excites a rovibrational overtone transition $(v=0, L) \rightarrow (v'=4, L')$. The HD^+ ions excited to the $v'=4$ vibrational level are dissociated using cw 266 nm laser radiation: $HD^+(v'=4)+h\nu \rightarrow H+D^+$, or $H^+ + D$. Due to different Franck-Condon wavefunction overlap, the calculated UV absorption cross section from the $v'=4$ level ($\sim 2.4\times 10^{-17}$ cm^2) is about 7 orders of magnitude larger than from $v=0$ [68]. Energy values represent total binding energies of the molecule [69].

range were chosen so that the ion crystal had sufficient time to cool back to its initial temperature between individual excitation cycles. The excitation heats both the molecular ions and the atomic coolants, which changes the scattering rate of 313 nm cooling light by the Be^+ ions. The HD^+ secular resonance becomes visible in the Be^+ fluorescence, and its strength is proportional to the amount of HD^+ ions in the ion crystal.

4.2 Spectroscopy of HD^+

The choice of HD^+ for spectroscopic studies was made because of the availability of dipole-allowed ro-vibrational transitions which simplify the spectroscopic techniques. Nevertheless, vibrational spectroscopy in the electronic ground state in near-absence of collisions, as is the case for the present molecular ions ensembles, is faced with the difficulty that molecules excited to a vibrational level decay only slowly, implying very low fluorescence rates. As the fluorescence wavelengths are in the mid to far infrared, photon counting would require a sophisticated detection system. We circumvent this difficulty by applying the technique of $(1+1')$ resonance enhanced multiphoton dissociation (REMPD): the molecules are excited by an infrared (IR) laser and then selectively photodissociated from the upper vibrational state by a second, fixed-wavelength ultraviolet (UV) laser (Fig.11). The remaining number of molecular ions is the quantity measured as a function of the frequency of the IR laser. As the molecular sample is small (typ. 40-100 ions) the spectroscopy requires the spectra to be obtained by repeated molecular ion production and interrogation cycles. The lasers employed are a single-frequency, widely tunable diode laser at 1.4 μm (Agilent 81480A), and a resonantly frequency-doubled Yb:YAG laser at 266 nm. The IR laser linewidth

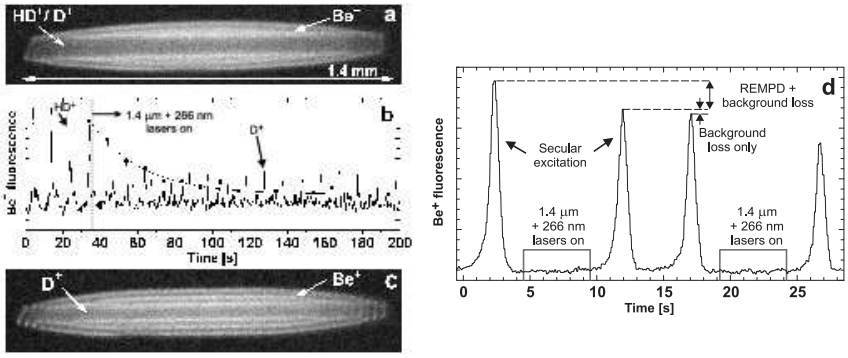

Fig. 12. (a) Initial ion crystal: ≈1100 Be^+, ≈100 HD^+, and ≈20 D^+ ions at ≈20 mK (the presence of cold HD^+ ions is obvious from the dark crystal core). (b) Repeated secular excitation of the crystal in (a) at 3 V amplitude. The excitation frequency was swept between 500 kHz and 1500 kHz. The IR laser is tuned to the maximum of the $(v = 0, L = 2) \rightarrow (v' = 4, L' = 1)$ line. The curve is an exponential fit with a decay constant of 0.04 s^{-1}. (c) Ion crystal after dissociation of all HD^+ ions: ≈1100 Be^+ and ≈50 D^+ ions at ≈20 mK. (d) Measurement cycle consisting of repeated probing of the number of HD^+ ions before and after exposure to the spectroscopy lasers [69].

was ∼5 MHz, and its frequency was calibrated with an accuracy of 40 MHz by absorption spectroscopy in a water vapor cell.

Due to the weak coupling between external and internal (rotational) degrees of freedom, the internal temperature of the HD^+ ions is close to room temperature, in thermal equilibrium with the vacuum chamber [70,10]. There is significant (>5%) population for rotational levels up to $L=6$. Indeed, we have observed 12 transitions between 1391 nm and 1471 nm, from lower rotational levels $L=0$ to $L=6$.

The loss of HD^+ ions not only depends on the REMPD process, but also on transitions induced by blackbody radiation (BBR). We modeled the loss of HD^+ by solving the rate equations for the populations of all (v, L) levels interacting with the IR and UV lasers, as well as with the BBR radiation at 300 K. The theoretically obtained excitation spectrum (see Fig. 13 and text below) of the levels probed by the IR laser is included, but for the remainder of the calculation hyperfine structure, due to electron, nuclear and rotational spins, is ignored. The rovibrational transition moments involved are taken from [71]. The rate of dissociation by UV light is obtained using cross sections from [68]. For typical UV intensities, dissociation rates of 10^2–10^3 s^{-1} are found. The rate equation model reveals two different timescales at which the HD^+ number declines during a typical experiment. A first, fast (<1 s) decay occurs when the IR laser selectively promotes HD^+ ions from a specific $(v=0, L)$ level to a rotational level in $v'=4$, from which they are efficiently photodissociated. This process rapidly dissociates those $(v = 0, L)$ HD^+ ions which are in the hyperfine states probed by the IR laser. The remaining molecular ions (a significant fraction of the total initial

number) are dissociated significantly slower, essentially at the rate at which the hyperfine levels of $(v = 0, L)$ are repopulated by BBR and spontaneous emission. For example, for the $(v = 0, L = 2) \rightarrow (v' = 4, L' = 1)$ transition, and for typical intensities of 6 W/cm^2 for the IR and 10 W/cm^2 for the UV laser, the fast HD^+ decay takes place at a rate $\sim$10 s^{-1} (which is not resolved experimentally), whereas the decay due to BBR–induced repopulation occurs at a rate of $\sim$0.04 s^{-1}. The latter rate is fairly consistent with the measured decay depicted in Fig.12(b), but observed decay rates depend strongly on which part of the hyperfine spectrum is interrogated. This points at a shortcoming of the simple rate equation model used here, and our observations can probably be explained precisely only by a rate equation model which takes the full hyperfine structure of all involved (v, L) levels into account.

As an example, Fig. 12(b) shows the time evolution of the HD^+ secular excitation resonance while the HD^+ ions are excited on the maximum of the rovibrational line $(v = 0, L = 2) \rightarrow (v' = 4, L' = 1)$ at 1430.3883 nm. The decrease of the HD^+ resonance in the secular excitation spectrum, induced by the REMPD process, is accompanied by a decrease of the dark crystal core containing the MHIs. The secular excitation spectrum also shows an increase of the number of D^+ ions, which result from the dissociation of excited HD^+ ions. These ions are sympathetically cooled and remain in the crystal core. Fig. 12(c) shows the mixed-species ion crystal after all HD^+ was dissociated. The dark crystal core has shrunk significantly, and the crystal now contains $\approx$1100 Be^+ and $\approx$50 D^+ ions. Assuming equal probability for photodissociation to D^+ and H^+, this number indicates that most generated D^+ ions are sympathetically cooled and trapped. Loss rates are obtained by exponential fitting to the maxima of the HD^+ resonances in the secular excitation spectrum (solid line in Fig. 12(b)). In this way, a 0.01 s^{-1} background loss rate of HD^+ ions from the trap is obtained when both the IR and UV lasers are turned off. This loss is due to chemical reactions between HD^+ ions and background gases. The observed background loss rate is fitted well by a single exponential decay, which rules out strong nonlinear dependence of the Be^+ fluorescence during secular excitation on the number of HD^+ ions.

The spectroscopic signal used to produce the spectra in Fig. 13 is the molecular ion dissociation probability, obtained as the relative change of the heights of the HD^+ secular resonances in the Be^+ fluorescence before and after the REMPD excitation (Fig. 12(d)). For each transition, the HD^+ dissociation probability was measured as a function of the frequency of the IR laser, in steps of 15 MHz. Each data point was obtained by averaging over several individual measurements of the HD^+ dissociation probability occurring over $\sim$5 s. Each data point requires a new loading of HD^+ ions in the Be^+ crystal. For all measurements, comparable HD^+ ion numbers were used, as deduced from the size of the crystal core after loading. However, during each HD^+ loading cycle a small fraction of the Be^+ is lost from the trap, due to chemical reactions with neutral HD gas [63]. The same Be^+ ion crystal can be used for up to 40 HD^+ loadings, sufficient for obtaining the spectra in Fig. 13. A typical spectrum is taken within 1-2 hours.

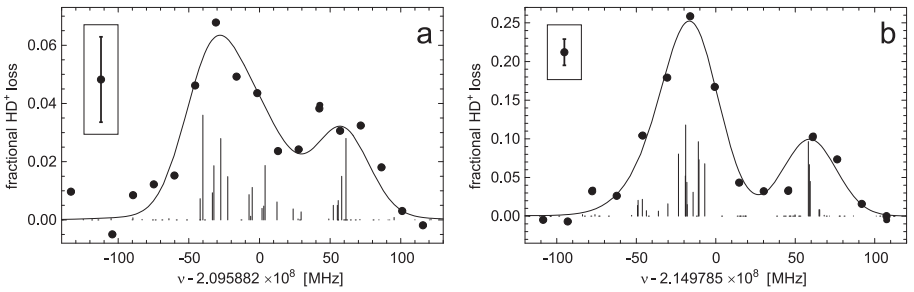

Fig. 13. Rovibrational transition spectra with partially resolved hyperfine splitting: (a) $(v=0, L=2) \rightarrow (v'=4, L'=1)$ at 1430 nm, (b) $(v=0, L=2) \rightarrow (v'=4, L'=3)$ at 1394 nm. The curves are fits to the data (•), where the theoretical stick spectra were broadened by ≈40 MHz. The theoretical spectrum exhibits a large number of very weak transitions, due to weak mixing of pure coupled angular momentum states. The ordinate values are the molecular ion dissociation probability for a 5 s irradiation of 0.65 W/cm^2 IR and 10 W/cm^2 UV light. The insets show typical error bars [69].

Detailed measurements for two transitions $(v=0, L=2) \rightarrow (v'=4, L'=1,3)$ are shown in Figs. 13(a,b). Both spectra reveal a partly resolved hyperfine structure, which can be compared with the prediction from an effective spin Hamiltonian, written as $H_{\rm eff} = b_1 \mathbf{I}_p \cdot \mathbf{S} + c_1 I_{pz} S_z + b_2 \mathbf{I}_d \cdot \mathbf{S} + c_2 I_{dz} S_z + \gamma \mathbf{S} \cdot \mathbf{J}$ [72,73]. Here, $\mathbf{I}_p$, $\mathbf{I}_d$, and $\mathbf{S}$ denote the spin of the proton, deuteron, and electron, respectively; the subscript z indicates the projection on the internuclear axis. The hyperfine coefficients b_1, b_2, c_1, c_2, and γ have been recently calculated to high accuracy [43], see Sec. 2.4. The hyperfine level energies and eigenfunctions are found by diagonalization of the matrix representation of $H_{\rm eff}$ in a suitable angular momentum coupling scheme. Terms arising from the nuclear spin-rotation and deuteron quadrupole interactions are neglected as they contribute $\ll$1 MHz to the hyperfine level energies [43]. The results of the diagonalization were subsequently used to calculate line strengths (Eq. 11) of the individual hyperfine components within a given rovibrational transition, leading to "stick spectra", as shown in Fig. 13. Inhomogeneous broadening of the spectra may be accounted for by convolving each line with a Gaussian lineshape of a given width.

The broadened stick spectra are fitted to the experimental spectra using the linewidth, the vertical scale and the frequency offset as fit parameters (Fig. 13). The frequency offset corresponds to the deperturbed ro-vibrational transition frequency, which is thus determined to within the accuracy of the wavelength calibration of the IR laser (40 MHz) and the fit uncertainty (3 MHz). The measured deperturbed ro-vibrational transition frequency is in good agreement with the *ab initio* results from [21], see Fig. 13. The partly resolved hyperfine structure in the measured spectra agrees well with the theoretical results obtained from [72,43]. We find both theoretically and experimentally that the hyperfine structure for other transitions in the P and R branches is similar to that in Figs. 13(a,b).

We observe a typical line broadening of 40 MHz, which corresponds to $k_B \times (0.2\,\mathrm{K})$ of energy in the axial motion. The kinetic energy in the secular motion (as inferred from molecular dynamics simulations) of the HD^+ ions can give rise to broadening of about 10 MHz only [61]. Saturation broadening also does not play a significant role, as confirmed by comparing spectra taken at different IR and UV intensities. Using the polarization-dependent 313 nm fluorescence of the Be^+ ions as a magnetic field probe, the magnetic field (which is along the direction of propagation of the 313 nm laser beam) has been adjusted and verified to be 50 mT and to vary by no more than 40 mT over the extent of the crystal, which implies Zeeman broadening <1 MHz. This leaves Doppler broadening due to micromotion as the most probable cause for the observed line broadening. This micromotion could arise from phase shifts in the rf potentials applied to the various electrodes, and from coupling between axial (IR laser beam direction) and radial ion motion. For our trap, in which the HD^+ ions are located at least 10 μm away from the trap axis, the (radial) micromotion energy exceeds $k_B(0.5\,\mathrm{K})$.

The results described are of significance in several respects. They demonstrate, for the first time, the possibility of high-resolution spectroscopy of small, trapped molecular ion samples, sympathetically cooled well into the millikelvin range. We have achieved a spectral resolution 10 times higher than with any previous cold molecular ion method, and the same enhancement was obtained for the excitation rate. The observed population dynamics demonstrated the weakness of collisions. The methods used for trapping, cooling and detection are quite general, and are applicable to a host of other molecular ion species. This includes other ions of astrophysical and cosmological interest such as H_3^+ and its isotopomers, which have been trapped in our setup [61,62]. Also, the spectral resolution achieved here may be further improved: for instance, first-order Doppler broadening may be circumvented by use of a tightly confining trap which holds the ions in the Lamb-Dicke regime, or by two-photon spectroscopy. Furthermore, the presence of the atomic coolant ions offers an in situ tool to detect possible perturbing fields.

5 Conclusion and Outlook

In summary, the development of high-accuracy laser spectroscopy of trapped MHIs has made significant progress. On the theory side, the energies have been calculated with a relative accuracy of the order of 1 ppb. Detailed predictions of the line strengths of one- and two-photon transitions have been given, which are important guides for the experiments. Certain systematic shifts (dc and ac Stark shifts [15,22]) have also been calculated, but are not described here. On the experimental side, several important techniques have been demonstrated: cooling of MHIs to tens of mK, vibrational-state selective photodissociation, one-photon vibrational spectroscopy with spectral resolution at the level of $2{\cdot}10^{-7}$, rotational population measurement, in-situ ion detection, tunable, high-power, continuous-wave narrow-linewidth laser for two-photon spectroscopy. Based on the present

results, it is expected that the two-photon H_2^+ spectroscopy experiment will ultimately allow a spectral resolution at the level of $3 \cdot 10^{-10}$, while the one-photon $1.4\,\mu$m HD^+ spectroscopy in the current apparatus will be limited by Doppler broadening to several parts in 10^8. One-photon spectroscopy of HD^+ vibrational transitions having longer wavelength or the use of a trap with stronger confinement should allow reaching the Lamb-Dicke regime, with a strong increase in spectral resolution. As described above, two-photon spectroscopy is another alternative.

For both ion species, the investigation of systematic shifts will become an important task. It is expected that Zeeman shifts and Stark shifts can be reduced or measured to a level below one part in 10^{10} in a cold ion ensemble. This should enable comparisons of experimental and theoretical transition frequencies at levels below 1 ppb, and, in the longer term, the development of a novel approach to the measurement of mass ratios of electron and hydrogen isotopes.

In the future, it may become attractive to use the method of quantum-logic-enabled spectroscopy [74,75]. Some of the experimental limitations (broad state population distribution, need for destructive detection of molecular excitation, systematic effects) encountered with the approaches described here could be substantially alleviated.

Acknowledgements

We thank P. Blythe and H. Daerr for their contributions and M. Okhapkin, A. Nevsky, I. Ernsting and A. Wicht for discussions and assistance. This work was supported by the German Science Foundation, the EC Network HPRN-CT-2002-00290 "Cold Molecules". We also thank S. Kilic, F. Bielsa, A. Douillet, T. Valenzuela and O. Acef for their contributions, as well as the LNE-SYRTE (Paris Observatory) and LPL (Université Paris 13) laboratories for lending IR optical components and their absolute frequency measurement setup. (J.K.) thanks the Alexander-von-Humboldt-Foundation for support. (V.K.) acknowledges support of RFBR, grant No. 05-02-16618.

References

1. C.A. Leach and R.E. Moss, *Annu. Rev. Phys. Chem.* **46**, 55 (1995).
2. see e.g. the DIREF database, http://diref.uwaterloo.ca; P.F. Bernath and S. McLeod, J. Mol. Spectrosc. **207**, 287 (2001).
3. K.B. Jefferts, Phys. Rev. Lett. **23**, 1476 (1969).
4. W.H. Wing, G.A. Ruff, W.E. Lamb, J.J. Spezeski, Phys. Rev. Lett. **36**, 1488 (1976).
5. A. Carrington, Science **274**, 1327 (1996), and references therein.
6. A.D.J. Critchley, A.N. Hughes, I.R. McNab, Phys. Rev. Lett. **86**, 1725 (2001).
7. J.J. Spezeski, Ph.D. thesis, Yale University (1977).
8. Y.P. Zhang, C.H. Cheng, J.T. Kim, J. Stanojevic, and E.E. Eyler, Phys. Rev. Lett. **92**, 203003 (2004), and references therein.
9. H. Schnitzler, Ph.D. dissertation, Univ. Konstanz (2001).
10. J.C.J. Koelemeij, B. Roth, and S. Schiller, in preparation (2006).

11. H. Müller, S. Herrmann, A. Saenz, A. Peters, C. Lämmerzahl, Phys. Rev. D **70**, 076004 (2004).
12. S. Schiller and V. Korobov, Phys. Rev. A **71**, 032505 (2005).
13. J.P. Uzan, Rev. Mod. Phys. **75**, 403 (2003).
14. D. DeMille, Phys. Rev. Lett. **88**, 067901 (2002).
15. L. Hilico, N. Billy, B. Grémaud, and D. Delande, Eur. Phys. J. D **12**, 449 (2000).
16. J.-Ph. Karr and L. Hilico, J. Phys. B **39**, 2095 (2006).
17. P.J. Mohr and B.N. Taylor, Rev. Mod. Phys. **77**, 1 (2005).
18. J. Verdu, S. Djekic, S. Stahl, T. Valenzuela, M. Vogel, G. Werth, T. Beier, H.J. Kluge, W. Quint, Phys. Rev. Lett. **92**, 093002 (2004).
19. S.G. Karshenboim, Phys. Reports **422**, 1 (2005).
20. R.E. Moss, Molecular Physics **80**, 1541 (1993).
21. R.E. Moss, Molecular Physics **78**, 371 (1993).
22. J.-Ph. Karr, S. Kilic, and L. Hilico, J. Phys. B **38**, 853 (2005).
23. V.I. Korobov, Phys. Rev. A **61**, 064503 (2000).
24. D.H. Bailey and A.M. Frolov, J. Phys. B **35**, 4287 (2002).
25. Zong-Chao Yan, Jun-Yi Zhang, and Yue Li, Phys. Rev. A **67**, 062504 (2003).
26. M.M. Cassar and G.W.F. Drake, J. Phys. B **37**, 2485 (2004).
27. A.M. Frolov and V.H. Smith, Jr. J. Phys. B **28**, L449 (1995).
28. V.I. Korobov, J. Phys. B **35**, 1959 (2002); F.E. Harris A.M. Frolov, and V.H. Smith, Jr., J. Chem. Phys. **121**, 6323 (2004).
29. H.A. Bethe and E.E. Salpeter, *Quantum mechanics of one– and two–electron atoms*, Plenum Publishing Co., New York, 1977.
30. V.B. Berestetsky, E.M. Lifshitz and L.P. Pitaevsky, *Relativistic Quantum Theory*, Pergamon, Oxford, 1982.
31. V.I. Korobov, Phys. Rev. A **74**, 052506 (2006).
32. K. Pachucki, J. Phys. B **31**, 3547 (1998).
33. A. Yelkhovsky, Phys. Rev. A **64**, 062104 (2001).
34. V.I. Korobov, Phys. Rev. A **70**, 012505 (2004).
35. V.I. Korobov, Phys. Rev. A **73**, 024502 (2006).
36. H. Araki, Prog. Theor. Phys. **17**, 619 (1957); J. Sucher, Phys.Rev. **109**, 1010 (1958).
37. V.I. Korobov and Ts. Tsogbayar, in preparation.
38. J.R. Sapirstein, D.R. Yennie, in: T. Kinoshita (Ed.), *Quantum Electrodynamics*, World Scientific, Singapore, 1990.
39. M.I. Eides, H. Grotch, and V.A.Shelyuto, Phys. Reports **342**, 63 (2001).
40. A.J. Layzer, Phys. Rev. Lett. **4**, 580 (1960).
41. K. Pachucki, Ann. Phys. (N.Y.) **226**, 1 (1993).
42. K. Pachucki, Phys. Rev. Lett. **72**, 3154 (1994); M.I. Eides and V.A. Shelyuto, Phys. Rev. A **52**, 954 (1995).
43. D. Bakalov, V.I. Korobov, and S. Schiller, Phys. Rev. Lett. (to be published).
44. V.I. Korobov, L. Hilico, and J.-Ph. Karr, Phys. Rev. A **74**, 040502(R) (2006).
45. D. Bakalov, V.I. Korobov, S. Schiller, In *Proceedings of the International Conference on exotic atoms "EXA 2005"*, February 21-25, 2005, Vienna, Austria.
46. B. Cagnac, G. Grynberg and F. Biraben, J. Physique **34**, 845 (1973); J.C. Garreau, M. Allegrini, L. Julien and F. Biraben, J. Physique **51**, 2275 (1990).
47. L. Hilico, N. Billy, B. Grémaud and D. Delande, J. Phys. B **34**, 491 (2001).
48. A.V. Matvijenko and L.I. Ponomarev, J. Phys. B **5**, 27 (1972); J. Carbonel, R. Lazauskas, D. Delande, L. Hilico, S. Kilic, Europhysics Letter **64**, 316 (2003).
49. A. Carrington *et al.*, J. Chem. Soc. Faraday Trans. **89**, 603 (1993); A. Carrington, C.A. Leach, and M.R. Viant, Chem. Phys. Lett. **206**, 77 (1993).

50. G.H. Dunn, Phys. Rev. **172**, 1 (1968). JILA report **92** (1968).
51. Senem Kilic, thèse de l'université Pierre et Marie Curie (Paris 6), 2005.
52. Y. Weijun, R. Alheit, G. Werth, Z Physik D **28**, 87 (1993).
53. L.S. Rothman *et al.*, J. Quant. Spec. Rad. Tr **96**, 139 (2005).
54. R.M. Williams *et al.*, Optics Letters **24**, 1844 (1999).
55. M.S. Taubman *et al.*, Optics letters **27**, 2164 (2002).
56. F. Bielsa, T. Valenzuela, A. Douillet, J.-Ph. Karr, and L. Hilico, submitted to Optics Letters.
57. F. Bielsa, K. Djerroud, A. Goncharov, T. Valenzuela, A. Douillet, C. Daussy, A. Amy-Klein, L. Hilico, submitted to J. Mol. Spec.
58. A. Amy-Klein *et al.*,Optics Letters **30**, 3320 (2005).
59. D.J. Larson *et al.*, Phys. Rev. Lett. **57**, 70 (1986).
60. K. Molhave and M. Drewsen, Phys. Rev. A **62**, 0011401(R) (2000).
61. P. Blythe *et al.*, Phys. Rev. Lett. **95**, 183002 (2005).
62. B. Roth *et al.*, J. Phys. B **39**, S1241 (2006).
63. B. Roth *et al.*, Phys. Rev. **A 73**, 042712 (2006).
64. A. Ostendorf *et al.*, to appear in Phys. Rev. Lett. (2006).
65. H. Schnitzler *et al.*, Applied Optics **41**, 7000 (2002).
66. B. Roth, A. Ostendorf, H. Wenz, and S. Schiller, J. Phys. B **38**, 3673 (2005).
67. B. Roth, P. Blythe, and S. Schiller, submitted to Phys. Rev. A (2006).
68. M. Tadjeddine and G. Parlant, Mol. Phys. **33**, 1797 (1977); A. Kondorskiy, private communications (2006).
69. B. Roth, J.C.J. Koelemeij, H. Daerr, and S. Schiller, Phys. Rev. A **74**, 040501(R) (2006).
70. A. Bertelsen, S. Jorgensen, and M. Drewsen, J. Phys. B **39**, 83 (2006).
71. E.A. Colbourn and P.R. Bunker, J. Mol. Spect. **63**, 155 (1976).
72. R.D. Ray and P.R. Certain, Phys. Rev. Lett. **38**, 824 (1977).
73. A. Carrington, I. McNab, and C. Montgomerie, J. Phys. B **22**, 3551 (1989).
74. D.J. Wineland *et al.*, in *Proceedings of the 6th Symposium on Frequency Standards and Metrology*, edited by P. Gill, World Scientific, Singapore, p. 361 (2002).
75. P.O. Schmidt *et al.*, Science **309**, 749 (2005).